Author Manuscript
Accepted for publication in a peer-reviewed journal

NIST National Institute of Standards and Technology • U.S. Department of Commerce

Published in final edited form as:
Soft Matter. 2017 October 04; 13(38): 6761–6769. doi:10.1039/c7sm00950j.

Weld formation during material extrusion additive manufacturing[1]

Jonathan E. Seppala[1], **Seung Hoon Han**[1,2], **Kaitlyn E. Hillgartner**[1,3], **Chelsea S. Davis**[1,4], and **Kalman B. Migler**[1]

[1]Materials Science and Engineering Division, National Institute of Standards and Technology, Gaithersburg, MD 20899, USA

[2]Montgomery College, Rockville, MD 20850, USA

[3]Chemical and Biological Engineering, Colorado School of Mines, Golden, CO 80401, USA

Abstract

Material extrusion (ME)[2] is a layer-by-layer additive manufacturing process that is now used in personal and commercial production where prototyping and customization are required. However, parts produced from ME frequently exhibit poor mechanical performance relative to those from traditional means; moreover, fundamental knowledge of the factors leading to development of inter-layer strength in this highly non-isothermal process is limited. In this work, we seek to understand the development of inter-layer weld strength from the perspective of polymer interdiffusion under conditions of rapidly changing mobility. Our framework centers around three interrelated components: in-situ thermal measurements (via infrared imaging), temperature dependent molecular processes (via rheology), and mechanical testing (via mode III fracture). We develop the concept of an *equivalent isothermal weld time* and test its relationship to fracture energy. For the printing conditions studied the equivalent isothermal weld time for T_{ref} = 230 °C ranged from 0.1 ms to 100 ms. The results of these analysis provide a basis for optimizing inter-layer strength, the limitations of the ME process, and guide development of new materials.

Introduction

Additive manufacturing, commonly called *3D printing*, is rapidly gaining use in many production sectors.[2] Although it is a decades old technology[3], a surge in adoption and development, spurred by expiring patents, inexpensive microprocessors, and internet driven file sharing is under way. In the material extrusion (ME) space, numerous printer designs exist, however, the underlying layout is the same, relying on a simple extrusion head pushing a solid thermoplastic filament through a heated extrusion nozzle, which moves along a prescribed three dimensional pattern relative to a build plate.[4] During the printing process a thermoplastic melt is extruded in successive layers, producing a three dimensional part of

[1]Official contribution of the National Institute of Standards and Technology; not subject to copyright in the United States.

[2]Material extrusion is the ASTM definition for this process[1], however, it is also known as fused deposition modeling® (FDM) or fused filament fabrication (FFF).

[4]Current Address: School of Materials Engineering, Purdue University, West Lafayette, IL 47907, USA

user-defined shape (see Figure 1). This technology may impact industries where low volume, personalized production, or features inaccessible in traditional manufacturing are key. Examples from the medical industry are numerous as patients typically need personalized designs such as, implants[5–8], prosthetics[9–13], and orthotics[14–17]. Surgical models for both surgeons and patients have already seen extremely positive results.[18] There are also clear use cases for small volume manufacturing in the aerospace industry[19] and manufacturing at point-of-need in defense and space.

The underlying sub-processes of ME are melting, extrusion and welding, all of which are well studied[20], however there are crucial differences in ME compared to the traditional processes in terms of kinetics, gradients, and time scales[21]. At a fundamental level, the challenge is to understand how to apply our knowledge of these processes to the highly non-isothermal kinetics of ME. One major difference between ME and traditional processing is the thermal and shear history experienced by the molten polymer as it exits the extruder head and is deposited onto the cooler layer below (see Figure 1). The molten polymer experiences a large shear gradient as it exits the extruder, and this extrudate then turns 90° due to the deposition and motion of the extruder head.[22] As the extrudate comes into physical contact with the layer below, it cools by transferring thermal energy into the sub-layer, simultaneously heating that layer, including the crucial interface between the two layers. The bottom of the printed layer (sometimes called a road) and the top of the one below each experience different highly non-isothermal processing conditions.

A second major difference concerns the development of part strength. While the importance of the inter-layer bonding was identified early in the development of this technology,[23] the underlying physics of the process has not been rigorously explored. Similar to extrusion, polymer-polymer welding has been studied for several decades[24–26] though primarily under isothermal conditions in the vicinity of the glass transition temperature. The process begins with surface wetting, followed by chains reptating across the interface creating frictional contacts, and eventually developing into entanglements.[27] The relationship between isothermal healing time and weld strength has been studied from experimental,[26,28–32] computational,[33–37] and theoretical[24,38–44] perspectives. It has been found that there is a time-temperature scaling relationship of approximately $t^{1/4}$ in amorphous polymers; this can be understood theoretically through a double reptation model. In a typical experiment weld strength steadily increases until it saturates at the bulk strength of the material. In the case of ME, the process is highly non-isothermal, as described above, and so a different concept of assessing the time-temperature relationship must be developed.

The underlying premise of the current work is that the development of weld strength can be considered as a problem of polymer-polymer interdiffusion that occurs in the immediate weld zone as a result of the temperature profile of that zone. This premise requires development of a three-pronged experimental framework of thermography, rheology and fracture mechanics.

First, we measure the temperature profile of the weld zone as a function of the primary experimental variables: extruder head temperature and print speed. In any thermoplastic process, temperature is a critical parameter in the control of the process and in the

understanding of the phenomena. It is critical to know how long the polymer spends at each temperature, because temperature is a critical parameter in determining polymer molecular mobility, especially for glassy polymers.

Second, we need to know the change in mobility of the polymer as a function of temperature so that we can build up the history of the mobility during each time step of the weld formation. This information can be obtained by measurement of the polymer rheology using small-amplitude oscillatory shear along with time-temperature superposition. Through repeated measurements at a set of temperatures, we can obtain the horizontal shift-factor a_T, whose inverse provides a relative measure of polymer mobility. Armed with data concerning the temperature as a function of time and the mobility as a function of temperature, we consider the weld process as being controlled by the polymer mobility as a function of time (until the polymer reaches its glass transition point where the reptational mobility goes to zero) similar to the work of Yang and Pitchumani[45]. We utilize the temperature data and the shift factors to construct an *effective isothermal weld time,* which we will relate to mechanical properties. Third, we select the mode III fracture test as our representative mechanical property. This is a useful test because it ensures fracture along the interlayer zone and it relates to a primary weakness of ME, i.e., part strength.

Materials & Methods[3]

Materials

We carry out the experiments using acrylonitrile butadiene styrene (ABS) because it exhibits a glass transition, it is commonly used for ME and it exhibits a compelling complexity in its multi-phase structure. We purchased filaments from Makerbot Industries (Brooklyn, NY) and used as received. The filament has a nominal diameter of 1.75 mm and is colored natural. Filaments are stored in an electronic desiccation cabinet at <1 % relative humidity and ambient temperature.

Material Extrusion

The primary criteria for the geometry of the part that is to be printed is that it must be amenable to both the infrared (IR) thermography and the fracture test. Similar to our recent work where we describe those techniques, here we print a vertical sheet that is 16 layers high, one extruder width wide (≈0.4 mm), and 200 mm long.[46] We printed over a range of temperatures (from 210 °C to 270 °C) and a range of print speeds (from 3 mm/s to 100 mm/s), where the print speed is defined as the velocity of the extruder assembly along the x-axis. The linear feed rate of the filament into the extruder is directly related to the print speed as is the apparent shear rate. The filament feed rate is calculated as a ratio of the filament cross section, $\pi/4\ (1.75\ \text{mm})^2 = 2.40\ \text{mm}^2$, to the road cross section, $0.3\ \text{mm} \times 0.4\ \text{mm} = 0.12\ \text{mm}^2$, or 20:1, along with a material dependent correction factor, 0.95 for ABS, dropping the ratio to 19:1. The printing is performed with a modified Replicator 2X (R2X) (Makerbot Industries, Brooklyn, NY). The R2X was modified by replacing the plastic

[3]Certain commercial equipment, instruments, or materials are identified in this paper in order to specify the experimental procedure adequately. Such identification is not intended to imply recommendation or endorsement by the National Institute of Standards and Technology, nor is it intended to imply that the materials or equipment identified are necessarily the best available for the purpose.

carriage and gantry components with aluminum versions. Print temperature, direction, and print speed were controlled by exporting the build from Makerbot Desktop to G-code. The G-code was edited to produce the desired tool paths and covered to the R2X native format, x3g, using the GPXUi (https://github.com/markwal/GpxUi) G-code to .x3g conversion post processer. The print direction was kept fixed (left-to-right from the perspective of the IR camera). The first layer was always printed with the default settings for ABS (230 °C, 30 mm/s) to ensure good adhesion to the build plate. The build plate was set to 110 °C and covered with Kapton film, which was wiped clean with toluene and allowed to dry prior to printing.

Thermography

IR thermography was recently shown to be an effective means to measure two-dimensional temperature profiles in ME[46]. In this methodology, the temperature of weld zone (W_i) is not measured directly, but is obtained from the average of the layer that is actively being printed (L_{i+1}) and the first sub-layer (L_i) or $W_i = (L_{i+1} + L_i)/2$.

Temperature profiles were acquired using a InSb IR camera (FLIR A6701sc) equipped with a 3900 nm notch filter with 400 nm bandwidth (Spectragon BP-3900-200 nm), a 50 mm lens, and 0.75 inch extender ring. The frame rate was set to 60 Hz and the integration time was set to 600 μs. Three pixel by three pixel regions of interest (ROI) were used to mark the center of each layer during the build process. The lens configuration results in each pixel corresponding to an approximately 30 μm by 30 μm square. Temperature profiles were taken at the center of the build. Using the IR camera required the front window/door to be open. Offline isothermal temperature-IR signal measurements were made to convert IR signals to temperature. A disk of polymer approximate 500 μm thick was prepared and placed a onto a Linkam hot stage. IR measurements were taken with the camera overhead at several temperatures and a monochromatic Plankian expression was used to fit the resulting temperature-IR signal curve. A detailed description of this process was recently published.[46] We did need to modify the previously published IR thermography protocol for the regime when print speed is below 10 mm/s, which was not previously investigated, see Supporting Information. Data sets for all the temperature profiles used in this work are included in the electronic supplemental information (ESI).

Rheology

Viscoelastic master curves were prepared by measuring frequency temperature sweeps of hot pressed ABS disks using a strain-controlled rotational rheometer (TA Instruments ARES-G2). The oscillatory stress was measured at a frequency range of 1 rad/s to 100 rad/s and 0.5 % strain every 20 °C from 130 °C to 270 °C. Time temperature superposition (TTS) was used to shift frequency data into a single master curve and the horizontal shift factor from TTS were fit to the Williams-Landel-Ferry (WLF)[47] equation. Frequency accuracy is ±5 % and modulus accuracy is ±8 % based on measurement of the manufacturer supplied poly(dimethyl siloxane) standard.

Mode III Fracture

Mode III fracture experiments were run on an RSA3 (TA Instruments, New Castle, DE). Samples were cut in half, across the welds, and a crack was started between layers 8 and 9. The crack was opened at 1 mm/s while measuring the normal force with the transducer in low range. Weld width was measured by microtoming a flat cross-section from the center of the print geometry and measuring the width under 10× magnification.[48] For a given temperature and extrudate velocity, the test was repeated at least 5 times. For comparison of the strength of the printed sample to that of a bulk sample, we employed a similar mode III test on a bulk sample, prepared from the same filament. The bulk sample was prepared by pressing strands of filament with 0.5 mm stainless steel shin stock in hot press at 170 °C and 50 kN for 120 s followed by 10 kN for 120 s resulting in rectangular sheets 0.47 mm ± 0.01 mm (standard deviation from 3 replicate measurements) thick.

Results and Discussion

In Figure 2 the reflection-corrected temperature profiles for the top 3 layers, denoted L_P, L_{P-1}, and L_{P-2}, from printing at an extrusion temperature (T_{ext}) of 210 °C and x-axis velocity (v_x) of 100 mm/s are presented. In this figure, t = 0 s refers to the time when the extruder head is directly above the ROI. Thus, the top layer (L_P) and the weld zone between L_P and L_{P-1} do not exist for t < 0 while L_{P-1}, and L_{P-2} do exist. There are several notable features of these temperature profiles. First, the overall timescale is set by the time that printing polymer is above the glass transitions temperature (T_g), which can be seen as being approximately 2 s. Next, the first sublayer L_{P-1} quickly jumps above T_g, reaching a peak temperature approximately 0.2 s after the printing layer makes contact. The second sublayer L_{P-2} never reaches a temperature above T_g, and it peaks slightly later, at approximately 1 s.

The goal of these IR thermometry measurements is to ascertain the temperature of the interlayer weld zones. However, direct measurement of these zones is problematic due to reflections and geometric considerations. Hence, we estimate the weld temperature by taking the average of the layer above and below. These are included in the figure; the top weld zone is denoted as W_1 and refers to the zone between L_P and L_{P-1}, and so on for successive layers. Similar to the print layer, the temperature in the first sublayer (W_1) drops below T_g within approximately 2 s. The next weld temperature (W_2) peaks around the same time as the first sublayer, approximately 0.2 s, and the temperature barely reaches T_g at its peak. Increasing T_{ext} shifts all of the profiles upward, extending the time above T_g (see Figure 2b). However, even with the increase, the cooling time to T_g is on the order of seconds and W_2 at its peak barely exceeds T_g. Varying v_x, Figure 2c, produces minor changes in the temperature profiles, however, the change is most dramatic at longer times when the temperature has dropped below T_g and no welding is possible.

At long times, t > 5 s, the temperature of the bottom plate plays an important role in the temperature of each layer and the sublayers become hotter than L_P. Overall the temperature profiles match those from our earlier work[46], other modeling[23], and thermocouple based measurements[49], typically resulting in cooling rates on the order of 100 °C/s. Note, we do not measure significant reheating of sublayers as subsequent ones are added; this is

attributed to the geometry of our sample lacking neighboring layers and long times between printing subsequent layers.

To make meaningful comparisons between different printing conditions we convert the non-isothermal temperature profiles into an *equivalent isothermal weld time*. To accomplish this conversion, offline rheological measurements were preformed to determine the relationship between temperature and the relaxation time of the ABS polymer used in this work. From oscillatory shear experiments over a wide range of temperatures, horizontal shift factors (a_T) can be determined using time-temperature superposition.[50] Ideally, horizontal shift factors relate all relaxation processes (or relaxation times) across a wide range of temperatures via Eqn 1.[50]

$$a_T(T)=\frac{\tau_i(T)}{\tau_i(T_0)} \quad \text{Eqn 1}$$

Continuous dynamic moduli (Figure 3a) and complex viscosity (Figure 3b) profiles with minimal vertical offsets and horizontal shift factors (Figure 3b inset) at a reference temperature (T_{ref}) of 230 °C were generated from a series of frequency sweeps using time-temperature superposition. ABS, being a composite material consisting of butadiene spheres in a styrene acrylonitrile matrix, does not have the typical linear homopolymer viscoelastic response.[51–54] At low frequency (0.1 rad/s to 1 rad/s), G' deviates significantly from a slope of 2, Figure 3a. The moduli overlap through 1 rad/s to 100 rad/s, preventing the extraction of a low frequency characteristic time scale. Above 100 rad/s, G' dominates G", resembling a typically linear homopolymer melt with a high frequency crossover occurring at approximately 10^6 rad/s. An estimate of the plateau modulus (G_N^0) from the minimum in tan(δ)[55] was determined to be 3.98×10^6 Pa, which would typically be used to estimate the disengagement time ($\tau_d, \eta_0 = 0.822 G_N^0 \tau_d$),[50] however, the complex viscosity does not exhibit a terminal viscosity (η_0), Figure 3b, instead continuing upward as frequency decreases. The ABS shear thins throughout the frequency range measured. Three print speeds are overlaid on the complex viscosity, falling in the mid-frequency range. To calculate the overlay points, the apparent wall shear rate ($\dot{\gamma}_{aw}$) for a given print speed was calculated from the volumetric flow rate (Q) at that print speed and the nozzle diameter (R) using Eqn 2.

$$\dot{\gamma}_{\mathrm{aw}}=\frac{4Q}{\pi R^3} \quad \text{Eqn 2}$$

A power law correction, Eqn 3,was applied to the apparent wall shear rate using a power law index of n = 0.32, fit from the slope of the complex viscosity in the mid-frequency regime (10^1 rad/s to 10^5 rad/s).

$$\dot{\gamma}_w=\frac{1}{4}\dot{\gamma}_{\mathrm{aw}}\left[3+\frac{1}{n}\right] \quad \text{Eqn 3}$$

Finally the Cox-Merz rule, $\eta(\dot{\gamma} = \omega) = |\eta^*|(\omega)$,[56] was applied to overlay the steady and dynamic values; adherence of ABS to the Cox-Merz rule has been experimentally verified.[51]

The WLF expression, Eqn 4 (C_1 = 4.65, C_2 = 200.9 °C, T_{ref} = 230 °C), fits $a_T(T)$ though all but the highest temperature, Figure 3b inset, providing a continuous value of a_T across the temperature range studied. Degradation at higher temperature is the most likely cause of the deviation (see SI Figure 3), this sets an upper limit to achievable temperature with this polymer. Both the viscoelastic response and the reference-temperature-corrected WLF constants (C_1, C_2) are in good agreement with those measured by Aoki and Nakayama.[54]

$$\log(a_T) = \frac{-C_1(T - T_r)}{C_2 + (T - T_r)} \quad \text{Eqn 4}$$

With the relationship between relaxation times and temperature established through rheological measurements, an *equivalent isothermal weld time* can be calculated.

a_T allows us to define a reduced time $t_r = t/a_T$, which relates times at different temperatures to time at the reference temperature and provides the basis for calculating the *equivalent isothermal weld time*, referred to here after as weld time (t_w). In this approach, the weld temperature profile is approximated as a series of isothermal temperatures. The reduced time for each isothermal step from the beginning of weld formation until T = T_g is calculated and the sum is t_w. Alternatively, the calculation is the same as numerical integration of $1/a_T$ with respect to t over the same time range, Eqn 5.

$$t_w = \int_0^{t_T = T_g} \frac{\mathrm{dt}}{a_T(t)} \quad \text{Eqn 5}$$

For example, the horizontal shift factor (a_T) is calculated at the estimated weld temperature (T_{ext} = 230 °C, v_x = 100 mm/s) using the WLF fit parameters, above, and plotted inversely against time, Figure 4. The area under the curve or weld time is calculated by numerically integrating Eqn 5 from t = 0 to t = 1.7 s (where $T_{weld} = T_g$), resulting in t_w = 0.115 ms at T_{ref} = 230 °C.

The weld time is quite sensitive to extrusion temperature, Figure 5; note t_w increases by approximately two orders of magnitude over the range of temperatures examined. The weld time is much less sensitive to feed rate however, decreasing only modestly with increased print speed. The increase of weld time with extrusion temperature is seen by considering that higher temperatures are associated with higher values of the inverse of a_T (Fig. 3). Thus, since t_w is the area under the curve in Figure 4, it increases with increasing temperature over the time of the weld. The inverse relationship between t_w and v_x is perhaps less apparent. Three factors contribute to the increase in t_w at lower v_x: 1) the total build time is significantly longer at slow speeds allowing more heat transfer from the build plate and a warmer overall build volume 2) radiant heat transfer from the extruder nozzle increases as the nozzle spends more time over a given build volume both before and after the layer is

deposited and 3) the residence time in the nozzle decreases with higher print speeds, which may lead to lower thermal mass in the extrudate. One point (T_{ext} = 250 °C, v_x = 3 mm/s) is a clear outlier, however, the same deviation appears in the tear energy, below. It is suspected that the printer did not print at the requested temperature.

The raw data from a mode III fracture experiment are shown in Figure 6; the fluctuations with time (position) are due to classic stick-slip crack propagation, and are observed under all conditions.

The force measurement from the mode III fracture test was converted into a tearing energy through Eqn 6, which relates the tearing force, F, and weld width, w, to a tearing energy E.

$$\mathrm{E}=\frac{2F}{w} \quad \text{Eqn 6}$$

An example of the cross section used to determine the weld width is shown in Figure 7; the weld widths are narrower than the nominal width of the extruded layer.

The resulting tear energies are plotted in Figure 8 for all T_{ext} and v_x examined and the trends in this plot are similar to those seen in the weld time plot (Figure 5). In general, increases in T_{ext} correspond to increases in tear energy. A small increase in tear energy is observed as print speed decreases, with the exception of T_{ext} = 210 °C and v_x = 100 mm/s, where a relatively large increase is observed at high feed rate, however the weld width of that sample is significantly lower than other extrusion temperatures at the same speed. The data at 270 °C is somewhat unreliable as numerous bubbles and defects occur; while these do not affect the thermography unless a defect appears in the ROI, a bubble can certainly decrease the tear energy making all but the 10 mm/s and 30 mm/s prints unreliable. Printing was unreliable at temperatures below 200 °C and often resulted in jamming. The few samples printed at 190 °C fracture readily during removal from the build plate or during clamping on the mode III stage due to weak bonding.

Now we are in a position to construct a plot of effective weld time against tear energy, which combines the information from thermography and rheology. The results are shown in Figure 9 for all T_{ext} and v_x. We also show the tear energy from a bulk pressed sample. Since we are reporting tear energy, the weld time is scaled with $t_w^{0.5}$ to aid in the comparison with the literature cited previously. First, we observe that the values are clustered around the extrusion temperature, except T_{ext} = 250 °C and v_x = 3 mm/s (filled symbol) discussed in the previous sections. This is a clear manifestation of the conclusion mentioned above, that the tear energy is rather sensitive to temperature, but less so to print speed, similar to the tensile results from Coogan and Kazmer.[57] As weld time increases the tear energy increases, however, the bulk value is not reached; it does not exceed 70 % of the bulk value. This underperformance is also seen in comparisons of injection molded and ME manufactured ABS tensile, flexural samples where ME samples are 30 % to 70 % the strength of injection counterparts[58], and in ULTEM[4] tensile samples where the z-axis tensile strength is 50 % of

[4]ULTEM is the registered tradename for poly(etherimide) produced by SABIC.

the injection molded counterpart.[59] We do not observe a plateau at short weld times, which might be expected somewhere below 0.1 $s^{0.5}$, which we ascribe to our inability to print at or below 200 °C and so we cannot access short enough relative weld times.

The failure to meet bulk value of fracture strength is an important issue in ME. It is unclear if this is a fundamental limitation of the technology, or if perhaps longer effective weld times are needed. There are several factors that may be contributing to the underperformance: 1) the ABS is degrading at the higher temperatures, this is evident in the rheological measurements, anecdotally based on prevalence of air bubbles, discoloration, and odor while printing at high temperatures, and thermal gravimetric analysis (see SI Figure 3). 2) it is unlikely that the temperature during printing is uniform along the weld width (y-axis), it is more likely that center maintains $T > T_g$ longer than the edges, contributing to a weld strength gradient in the transverse direction. 3) The shape of the part differs from the pressed sheet, the weld in the tear samples have lobes extending away from the weld/tear site, which may act like stress concentrators.

Of these issues, only number 2 is fundamental to the process and may be mitigated in other geometries. Issue number 1 is a fundamental material limitation and would not be observed in more heat resistant polymers. Issue number 3 is a sample geometry limitation, further study may provide a correction to this issue. Here we make the point that the temperature profiles of these layers are specific to the printing protocol and part geometry employed here. Other print protocols could lead to different results with respect to the time above T_g. Our geometry and protocol is optimized to uncover the essential physics of the weld process rather than to make a particular shape or part.

Conclusion

We have presented a framework for the understanding of the development of weld strength in materials extrusion based additive manufacturing by adapting existing understanding from isothermal measurements to the non-isothermal case of ME. The framework includes the following triad: thermal history, molecular mobility, and mechanical property testing of the weld zone. Our implementation of this framework consisted of IR thermography, small amplitude rheology, and mode III fracture. However, we wish to point out that all elements of this triad could be improved and adapted in future work. For example, the thermography leg could seek to understand the 3D nature of the thermal kinetics through a combined measurements and modeling approach. The rheological component could consider the large shear rates that occur just prior to interdiffusion, and finally other modes of fracture or strength could be considered. This framework further provides a basis for systematic exploration of molecular properties, such as molar mass and its distribution.

One intriguing challenge to the field made elsewhere and confirmed here is that the strength does not reach that of parts produced by bulk methods. Comparing to the classic isothermal polymer-polymer welding, a steady increase in weld strength is observed as weld time increases. However, we are unable to exceed a strength of more than 70 % of the bulk strength. We can speculate on the cause: perhaps we are unable to reach sufficiently large values of the effective weld time due to degradation at high temperature; perhaps shear

induced polymer alignment plays an important role, and possibly the geometry of the mode III fracture causes stress concentrations. Understanding the weld formation is important in several fronts, such as improving weld strength, predicting part performance, and development of new materials. Resolution of this issue will lead to advancements and confidence in the use of ME products.

Supplementary Material

Refer to Web version on PubMed Central for supplementary material.

Acknowledgments

The authors would like to acknowledge P. Olmsted, D. Dillard, and M. Robbins for helpful discussions regarding various aspects of this work.

Funding Sources

Funding was provided by the National Institute of Standards and Technology (NIST) Summer Undergraduate Research Fellowship (SURF) and NIST Montgomery College Internship programs.

References

1. ISO/ASTM 52900:2015(E). Standard Terminology for Additive Manufacturing.
2. Powley, T. [accessed January 19, 2017] 3D printing reshapes factory floor. https://www.ft.com/content/1de6deba-6897-11e3-bb3e-00144feabdc0
3. Kruth J-P, Leu MC, Nakagawa T. CIRP Ann. - Manuf. Technol. 1998; 47:525–540.
4. Gibson, Ian, Rosen, David W., Stucker, Brent. Additive Manufacturing Technologies. Springer; US: 2010.
5. Zopf DA, Hollister SJ, Nelson ME, Ohye RG, Green GE. N. Engl. J. Med. 2013; 368:2043–2045. [PubMed: 23697530]
6. Morrison RJ, Hollister SJ, Niedner MF, Mahani MG, Park AH, Mehta DK, Ohye RG, Green GE. Sci. Transl. Med. 2015; 7:285ra64.
7. Katschnig M, Arbeiter F, Haar B, van Campe G, Holzer C. Adv. Eng. Mater.
8. Panayotov IV, Orti V, Cuisinier F, Yachouh J. J. Mater. Sci. Mater. Med.
9. Rogers, Bill, Stephens, Sean, Gitter, Andrew, Bosker, Gordon, Crawford, Richard. J. Prosthet. Orthot. 2000; 12:97–100.
10. Rogers B, Bosker GW, Crawford RH, Faustini MC, Neptune RR, Walden G, Gitter AJ. Prosthet. Orthot. Int. 2007; 31:88–100. [PubMed: 17365888]
11. Herbert, Nicholas, Simpson, David, Spence, William D., Ion, William. J. Rehabiliation Res. Dev. 2005; 42:141–164.
12. Hsu LH, Huang GF, Lu CT, Hong DY, Liu SH. Prosthet. Orthot. Int. 2010; 34:37–45. [PubMed: 19947824]
13. Sengeh, David Moinina, Herr, Hugh. J. Prosthet. Orthot. 2013; 25:129–137.
14. Pallari JHP, Dalgarno KW, Woodburn J. IEEE Trans. Biomed. Eng. 2010; 57:1750–1756. [PubMed: 20211798]
15. Dombroski CE, Balsdon ME, Froats A. BMC Res. Notes. 2014; 7:443. [PubMed: 25015013]
16. Cook D, Gervasi V, Rizza R, Kamara S, Liu X. Rapid Prototyp. J. 2010; 16:189–193.
17. Telfer S, Pallari J, Munguia J, Dalgarno K, McGeough M, Woodburn J. BMC Musculoskelet. Disord. 2012; 13:84. [PubMed: 22642941]
18. Petzold R, Zeilhofer H-F, Kalender WA. Comput. Med. Imaging Graph. 23:277–284.
19. Gehm, Ryan. [accessed February 23, 2017] 3D-printed parts fly on Airbus A350 XWB and ULA rockets. http://articles.sae.org/14166/

20. Fried, Joel R. Polymer Science and Technology. Prentice Hall: PTR; 1995.
21. Seppala J. Express Polym. Lett. 2016; 10:788–788.
22. McIlory, Claire, Olmsted, Peter D. J. Rheol.
23. Li, Longmei, Gu, Peihua. Trans. NAMRISME. 2003; 31:613–20.
24. Wool RP. Comptes Rendus Chim. 2006; 9:25–44.
25. Wool RP. Soft Matter. 2008; 4:400.
26. Kline DB, Wool RP. Polym. Eng. Sci. 1988; 28:52–57.
27. Awaja F. Polymer. 2016; 97:387–407.
28. Jud K, Kausch HH, Williams JG. J. Mater. Sci. 1981; 16:204–210.
29. Shim M-J, Kim S-W. Mater. Chem. Phys. 1997; 48:90–93.
30. Akabori K-I, Baba D, Koguchi K, Tanaka K, Nagamura T. J. Polym. Sci. Part B Polym. Phys. 2006; 44:3598–3604.
31. Cho B-R, Kardos JL. J. Appl. Polym. Sci. 1995; 56:1435–1454.
32. Bousmina M, Qiu H, Grmela M, Klemberg-Sapieha JE. Macromolecules. 1998; 31:8273–8280.
33. Ge T, Robbins MO, Perahia D, Grest GS. Phys. Rev. E.
34. Ge T, Pierce F, Perahia D, Grest GS, Robbins MO. Phys. Rev. Lett.
35. Ge T, Grest GS, Robbins MO. Macromolecules. 2014; 47:6982–6989.
36. Pierce F, Perahia D, Grest GS. EPL Europhys. Lett. 2011; 95:46001.
37. Yokomizo K, Banno Y, Kotaki M. Polymer. 2012; 53:4280–4286.
38. Nayak NC, Yue CY, Lam YC, Tan YL. Microsyst. Technol. 2010; 16:487–491.
39. Allen KW. Polym. Int. 1995; 38:305–306.
40. Wool, RP. Polymer Interfaces: Structure and Strength. Hanser Publishers; 1995.
41. Lo C-T, Narasimhan B. Polymer. 2005; 46:2266–2275.
42. Benkoski JJ, Fredrickson GH, Kramer EJ. J. Polym. Sci. Part B Polym. Phys. 2002; 40:2377–2386.
43. Sperling LH, Klein A, Sambasivam M, Kim KD. Polym. Adv. Technol. 1994; 5:453–472.
44. Ezekoye OA, Lowman CD, Fahey MT, Hulme-Lowe AG. Polym. Eng. Sci. 1998; 38:976–991.
45. Yang F, Pitchumani R. Macromolecules. 2002; 35:3213–3224.
46. Seppala JE, Migler KD. Addit. Manuf. 2016; 12(Part A):71–76.
47. Williams ML, Landel RF, Ferry JD. J. Am. Chem. Soc. 1955; 77:3701–3707.
48. Davis CS, Hillgartner KE, Han SH, Seppala JE. Addit. Manuf. 2017; 16:162–166.
49. Sun Q, Rizvi GM, Bellehumeur CT, Gu P. Rapid Prototyp. J. 2008; 14:72–80.
50. Dealy, John M., Larson, Ronald G. Structure and rheology of molten polymers. Hanser Gardner Publications; Cincinnati:
51. Aoki Y. Macromolecules. 1987; 20:2208–2213.
52. Aoki Y. J. Non-Newton. Fluid Mech. 1986; 22:91–99.
53. Aoki Y. J. Rheol. 1981; 25:351–356.
54. Aoki Y, Nakayama K. Polym J. 1982; 14:951–958.
55. Liu C, He J, van Ruymbeke E, Keunings R, Bailly C. Polymer. 2006; 47:4461–4479.
56. Cox WP, Merz EH. J. Polym. Sci. 1958; 28:619–622.
57. Coogan, Timothy J., Kazmer, David Owen. Rapid Prototyp. J. 2017; 23:414–422.
58. Dawoud M, Taha I, Ebeid SJ. J. Manuf. Process. 2016; 21:39–45.
59. Fischer M, Schöppner V. JOM.

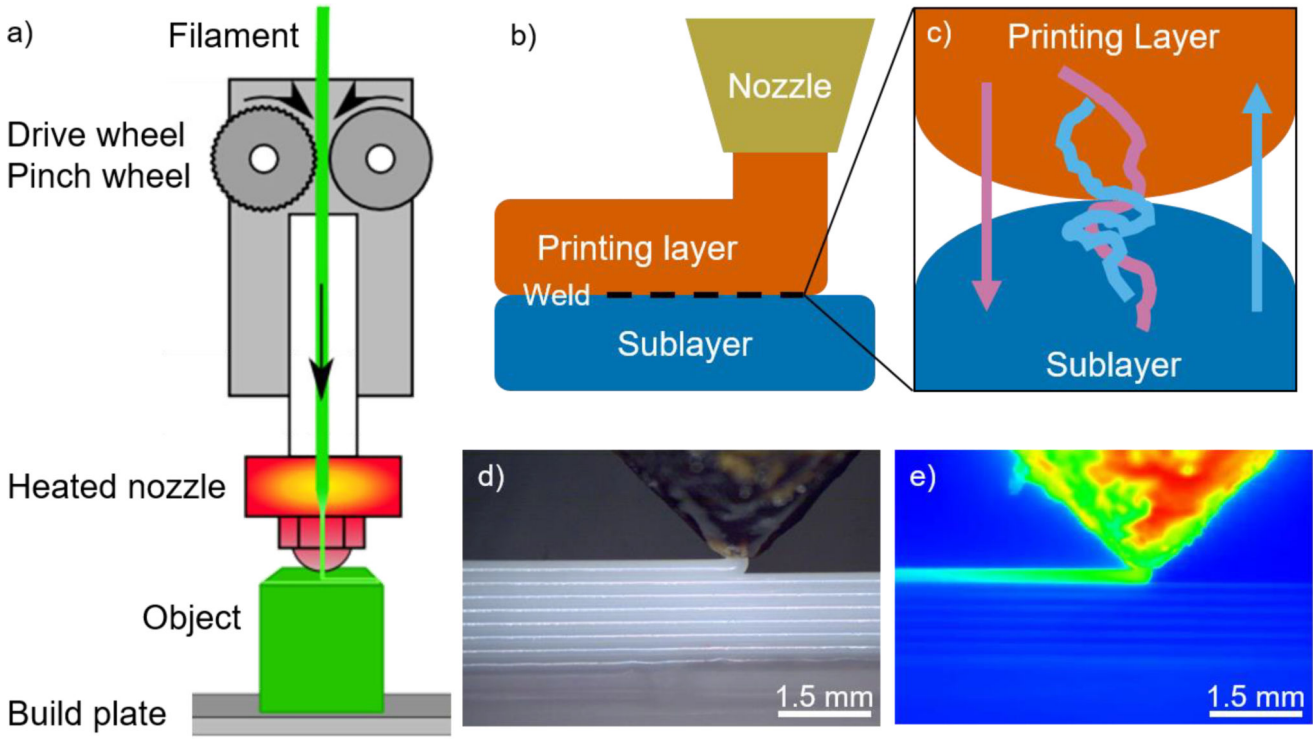

Figure 1.

Image of material extrusion 3D printing process a) illustration of extrusion components, b) illustration of process and weld location, c) illustration of weld formation and chain diffusion d) visible light image of printing process with 8 layers, and e) false color infrared image of printing process with 8 layers.

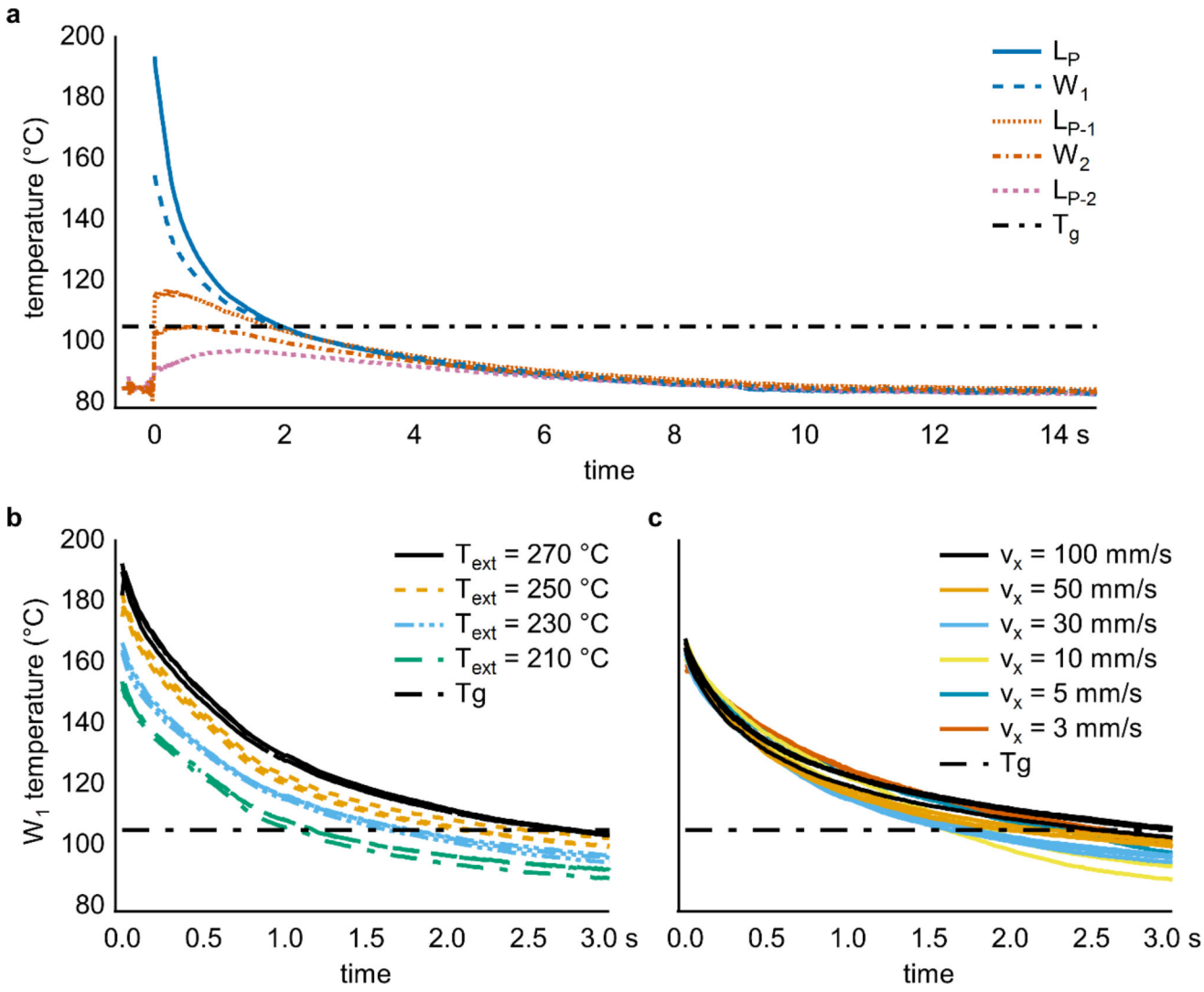

Figure 2.

a) Temperature profiles from layers formed during printing at T_{ext} = 210 °C and v_x = 50 mm/s. Print layer (L_P) temperature, first sublayer (L_{P-1}) temperature, second sublayer (L_{P-2}) temperature, estimate of weld temperature between print and first sublayer (W_1), estimate of weld temperature between first and second sublayers (W_2) and glass transition temperature for ABS (Tg). b) Weld temperature profile estimates at different T_{ext}, constant v_x = 30 mm/s. c) Weld temperature profile estimates with changing print speeds, isothermal T_{ext} = 230 °C.

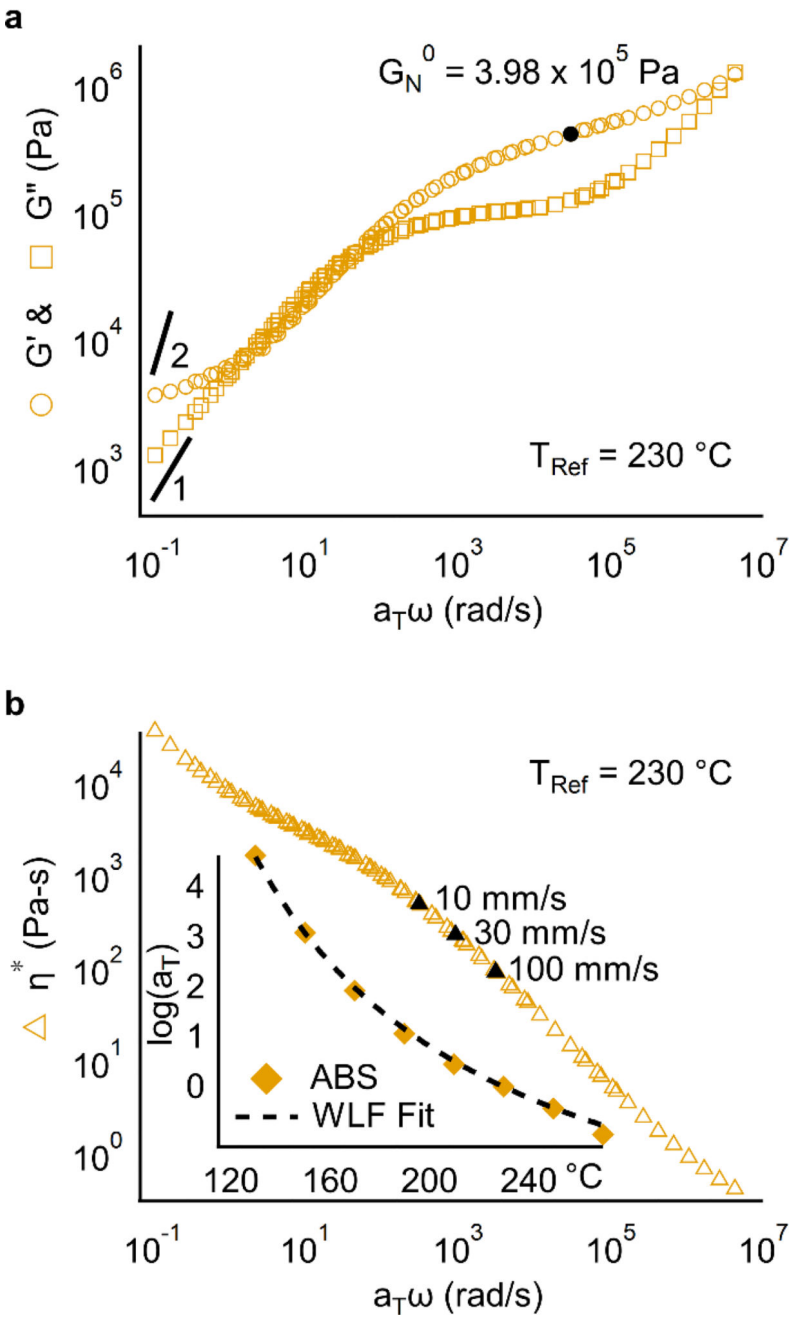

Figure 3.

Time-temperature superposition master curve of ABS from multiple frequency temperature sweeps. a) Storage modulus (G'), loss modulus (G"), and plateau modulus (G_N^0), determined from minimum of loss tangent.[55] b) Complex viscosity (η^*) with various prints speeds highlighted, inset: horizontal shift factors (a_T) and WLF fit.

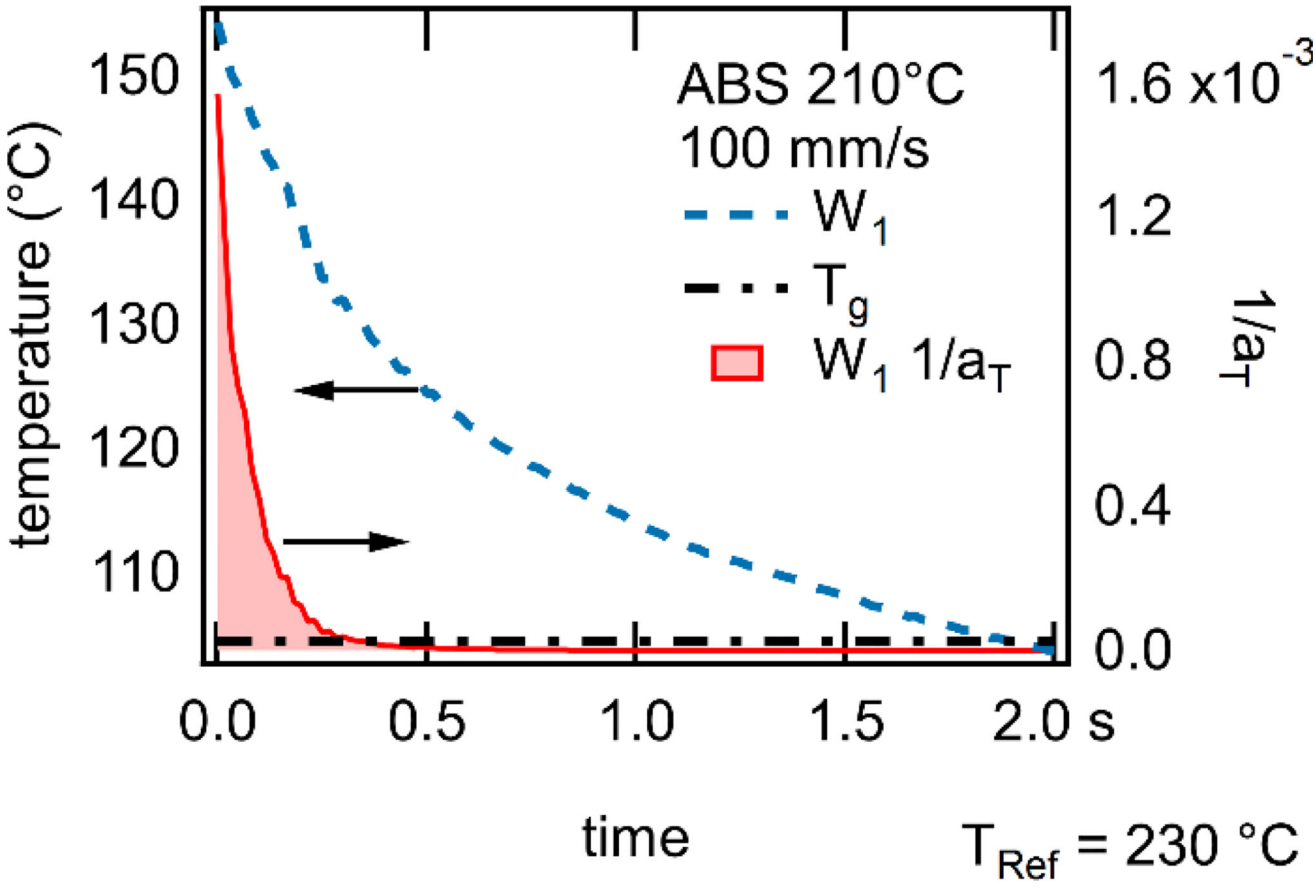

Figure 4.

Estimated weld temperature profile (left axis) and inverse horizontal shift factors, $1/a_T$, (right axis) for ABS printed at T_{ext} = 210 °C and v_x = 100 mm/s. Equivalent isothermal weld time corresponds to area under $1/a_T$ curve between start of print and T = T_g.

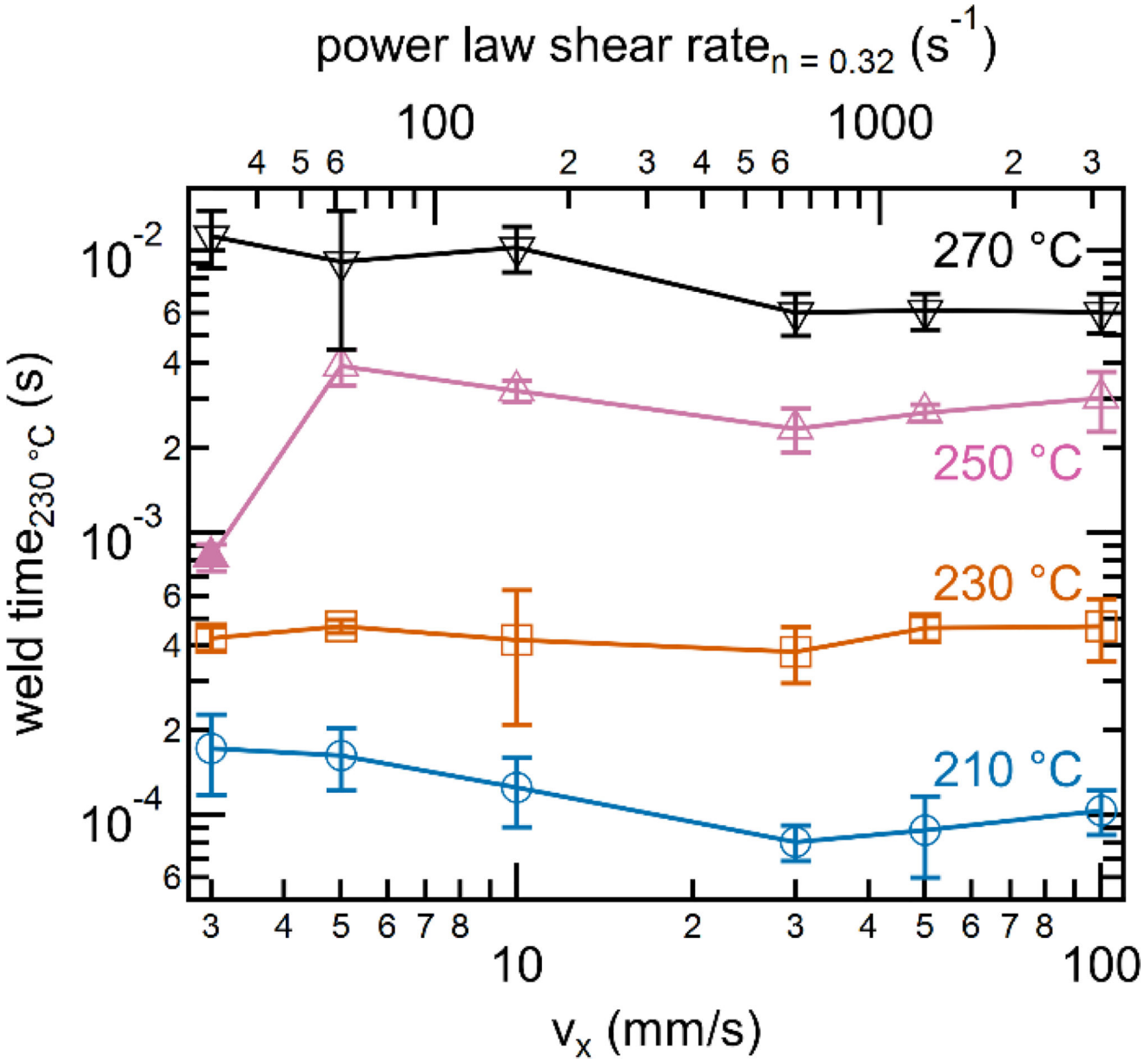

Figure 5.

Equivalent isothermal weld time, calculated by numerical integration of $1/a_T$ profiles determined from WLF fit to a_T values and temporal weld temperature profiles for all printing conditions studied. Error bars calculated from the standard deviation of 3 replicates. Power law shear rate determined from volumetric flow assuming n = 0.32.

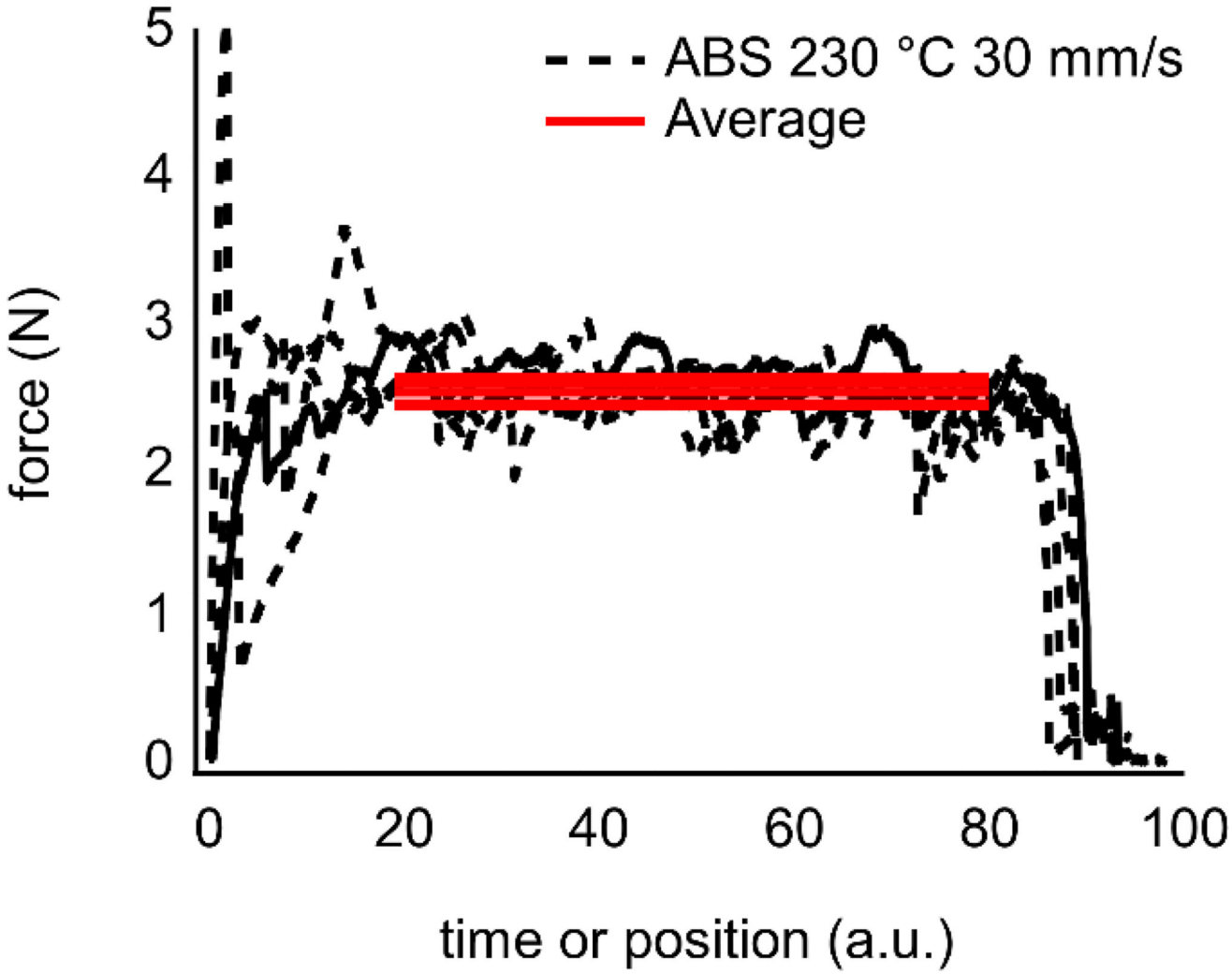

Figure 6.

Normal force measurements (black dashed) for a set of mode III fracture experiments from samples printed at T_{ext} = 230 °C and v_x = 30 mm/s and average value taken between fracture onset and end of test.

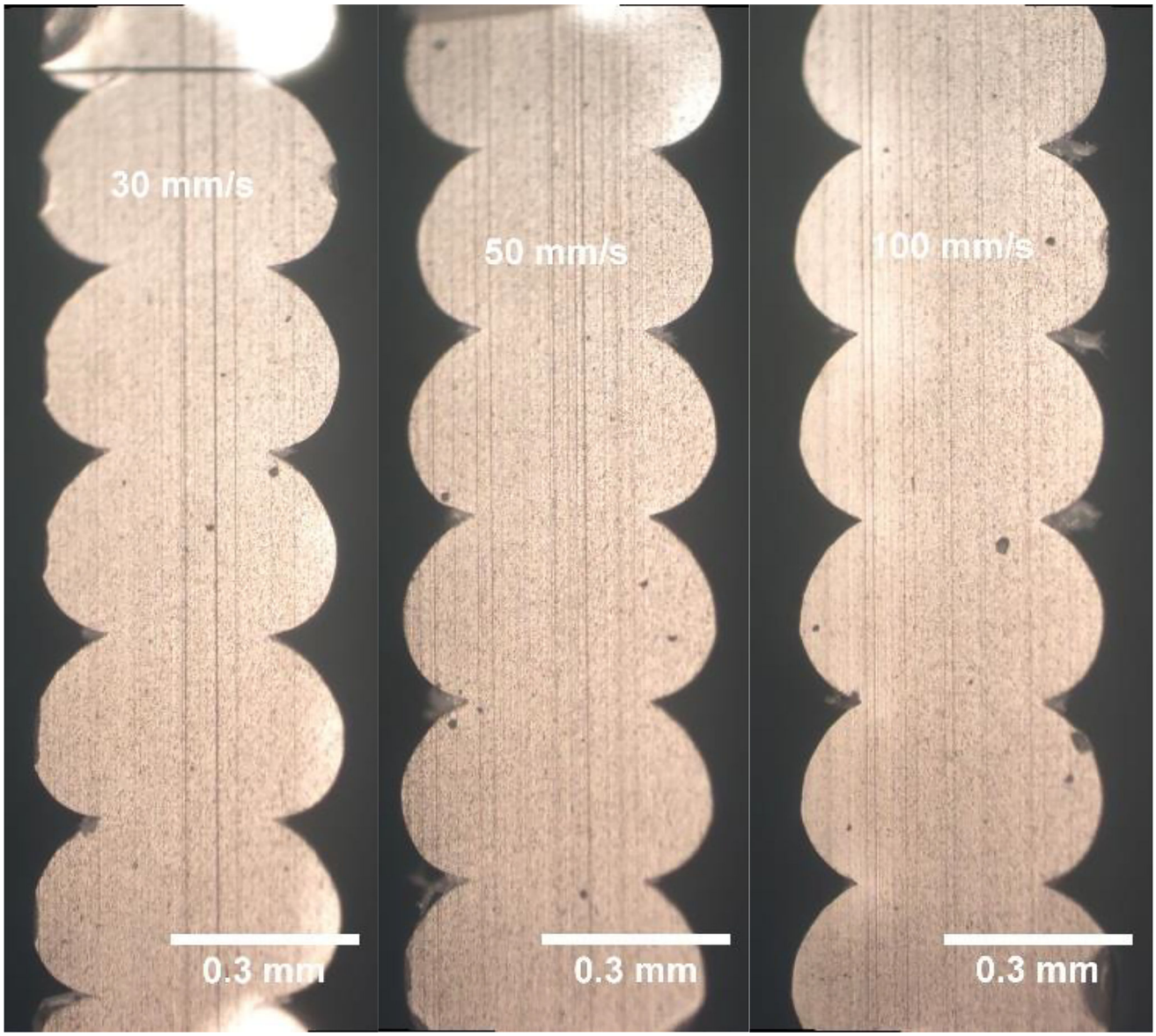

Figure 7.

Cross section of ABS welds at 10× magnification for printing conditions of T_{ext} = 230 °C and v_x = 30 mm/s, 50 mm/s and 100 mm/s. Weld widths were taken at the narrowest point between layers. Vertical striations are artifacts from microtoming samples.

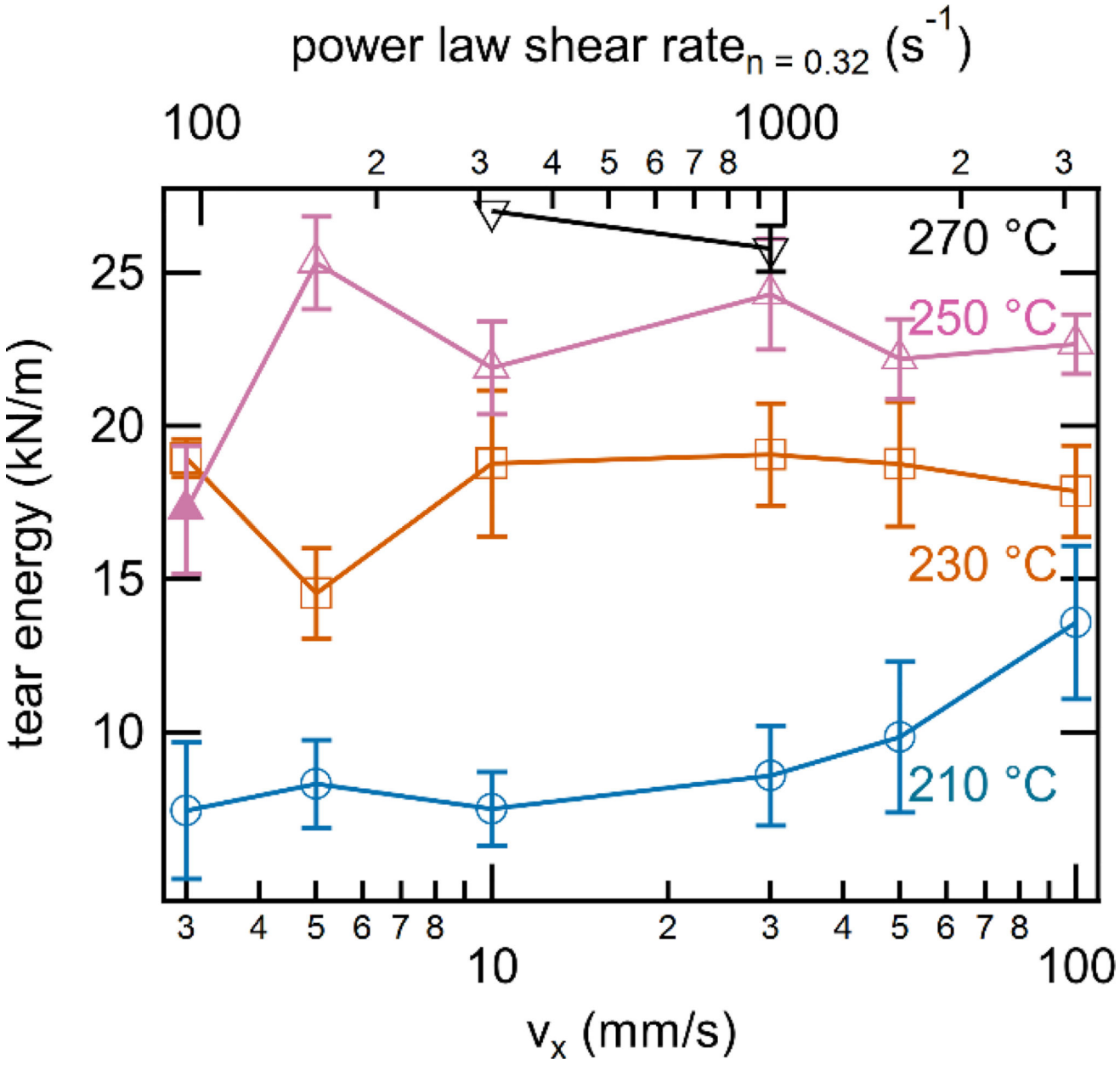

Figure 8.

Tear energy for all printing conditions studied. Results plotted with respect to x,y-translation speed or estimated shear rate. Error bars calculated from the standard deviation of 5 to 10 replicates.

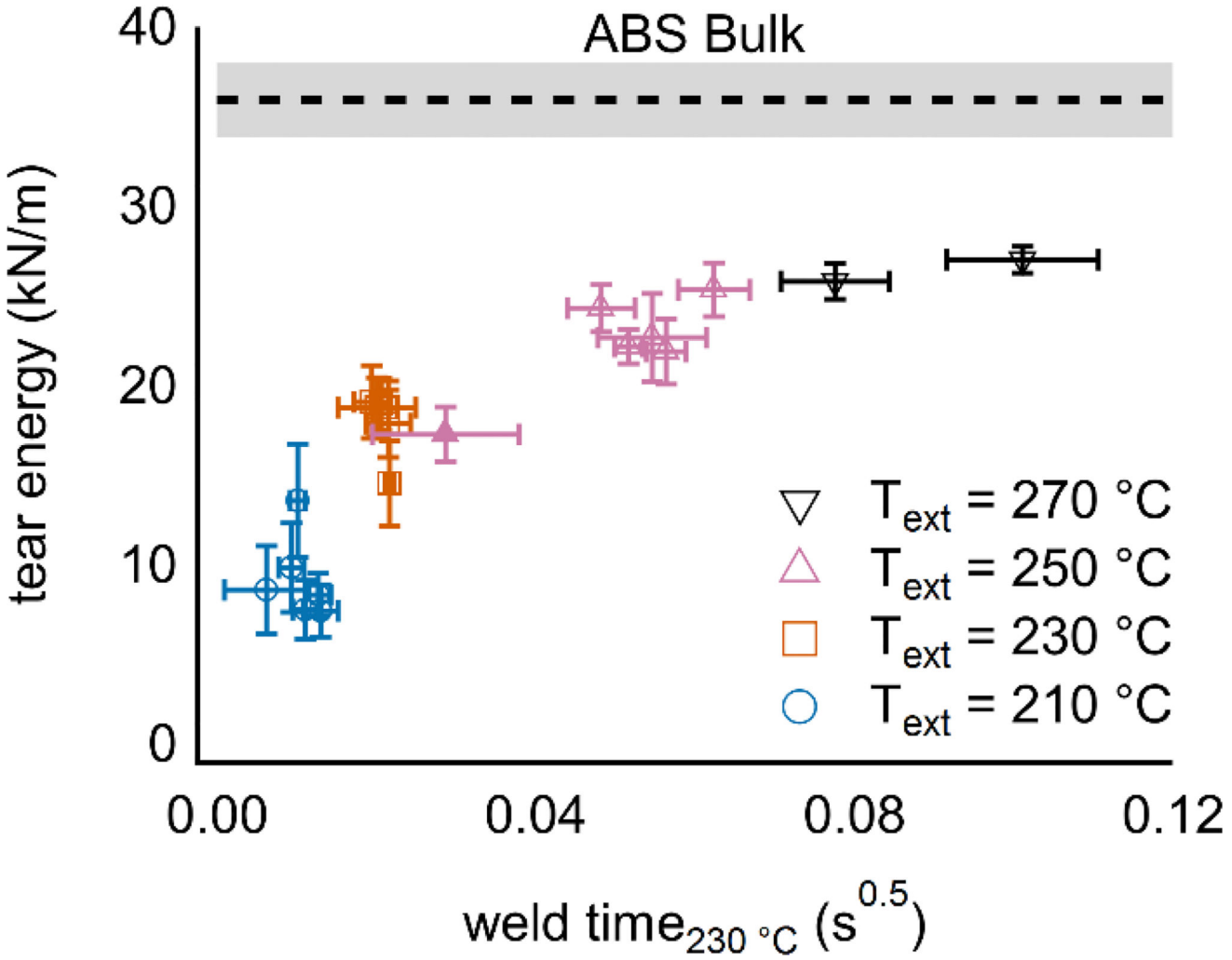

Figure 9.

Comparison of tear energy to equivalent isothermal weld time. At the top of the figure the bulk tear energy from a pressed ABS sheet. Horizontal error bars are calculated from the standard deviation of 3 replicates. Vertical error bars are calculated from the standard deviation of 5 to 10 replicates